PHYSICAL REVIEW B **102**, 024105 (2020)

High-precision equation of state data for TiO_2: A structural analog of SiO_2

Sakun Duwal,[*] Chad A. McCoy, Philippe F. Weck, Patricia Kalita, Heath L. Hanshaw,
Kyle Cochrane, Tommy Ao, and Seth Root
Sandia National Laboratories, Albuquerque, New Mexico 87125, USA

(Received 22 April 2020; accepted 29 June 2020; published 14 July 2020)

The high-pressure response of titanium dioxide (TiO_2) is of interest because of its numerous industrial applications and its structural similarities to silica (SiO_2). We used three platforms—Sandia's Z machine, Omega Laser Facility, and density-functional theory-based quantum molecular dynamics (QMD) simulations—to study the equation of state (EOS) of TiO_2 at extreme conditions. We used magnetically accelerated flyer plates at Sandia to measure Hugoniot of TiO_2 up to pressures of 855 GPa. We used a laser-driven shock wave at Omega to measure the shock temperature in TiO_2. Our Z data show that rutile TiO_2 reaches 2.2-fold compression at a pressure of 855 GPa and Omega data show that TiO_2 is a reflecting liquid above 230 GPa. The QMD simulations are in excellent agreement with the experimental Hugoniot in both pressure and temperature. A melt curve for TiO_2 is also proposed based on the QMD simulations. The combined experimental results show TiO_2 is in a liquid at these explored pressure ranges and is not highly incompressible as suggested by a previous study.

DOI: 10.1103/PhysRevB.102.024105

I. INTRODUCTION

TiO_2 is a 3*d* transition-metal oxide that garners interest from various fields ranging from solid-state physics and chemistry to geosciences. Solid-state physics and chemistry interests arise due to the many oxidation states in which Ti can exist and that TiO_2 is a wide-band semiconductor [1]. Geoscientists are especially attracted to TiO_2 because it is the low-pressure analog of the most abundant component of Earth's mantle, SiO_2 and the existence of different structural polymorphs of TiO_2 [2].

TiO_2 has three polymorphs at ambient conditions: rutile, anatase, and brookite with rutile being the most stable polymorph. Figure 1 shows the rutile TiO_2 phase diagram constructed from static high pressure studies [2–8] and *ab initio* calculations from this paper and others [9,10]. Although TiO_2 is a structural analog of SiO_2 [11,12], TiO_2 has significantly lower transition pressures than those of SiO_2. For example, in TiO_2 the α-PbO_2 phase stabilizes at 10 GPa, whereas the same phase does not stabilize until 100 GPa in SiO_2 [2]. Similarly, the cotunnite transition in TiO_2 is observed at 50 GPa, whereas this transition occurs at 680 GPa in SiO_2. The Fe_2P transition in TiO_2 occurs below 200 GPa, but occurs above 700 GPa in SiO_2. Intriguingly, the tenfold coordinated $I4/mmm$ structure in TiO_2 is predicted to occur above 650 GPa but is predicted to occur in excess of 10 TPa (10 000 GPa) in SiO_2 [10]—well beyond the capability of current experimental platforms.

Under shock compression, rutile TiO_2 undergoes three phase transitions (rutile $\Rightarrow$ low pressure phase, LPP $\Rightarrow$ high pressure phase, HPP I $\Rightarrow$ HPP II) along the Hugoniot, with the highest phase transition (HPP I $\Rightarrow$ HPP II) occurring around 100 GPa [9,13–17]. Al'tshuler *et al.* reported the highest shock pressures up to 292 GPa. Interestingly in the Al'tshuler data, as the shock pressure increases above 110 GPa in the HPPII phase, TiO_2 becomes highly incompressible. This leads to the interpretation that TiO_2 is virtually incompressible at high pressures on the Hugoniot [18]. In that same paper, Al'tshuler reported that CaF_2 also became incompressible at approximately 100 GPa. However, recent work by Root *et al.* [19] and Shu *et al.* [20] contradict the Al'tshuler findings and demonstrate that CaF_2 is not incompressible along the Hugoniot. Thus, an explanation as to why TiO_2 would have such behavior at moderately high pressure is lacking and further phase behaviors at higher pressures remain unexplored.

Today, advanced high-energy density facilities routinely achieve multimegabar pressure ranges in the laboratory. In this paper, we examine the shock compression behavior of rutile TiO_2, using the combination of three different, well-established platforms: the Sandia Z machine, the Omega Laser Facility, and density-functional theory (DFT)-based quantum molecular dynamics (QMD) simulations. We used magnetically accelerated flyer plates at Sandia's Z facility and laser-driven decaying shocks at the Omega facility. Both Z machine and Omega have a history of providing high-fidelity equation of state (EOS) measurements, but only a few studies have actually combined results from both platforms to obtain complete EOS of materials in P-T-ρ space [21]. Additionally, QMD simulations complement the experimental studies by providing information about the phase state and the melt boundary. Here, the combined data provide complete EOS data in density, pressure, and temperature space for TiO_2 at extreme conditions.

II. Z EXPERIMENTAL METHODS

To accurately measure the Hugoniot state, we conducted a series of magnetically accelerated flyer-plate shock compression experiments using Sandia's Z machine. The Z machine is the world's largest pulsed power facility capable of generating

---

[*] sduwal@sandia.gov

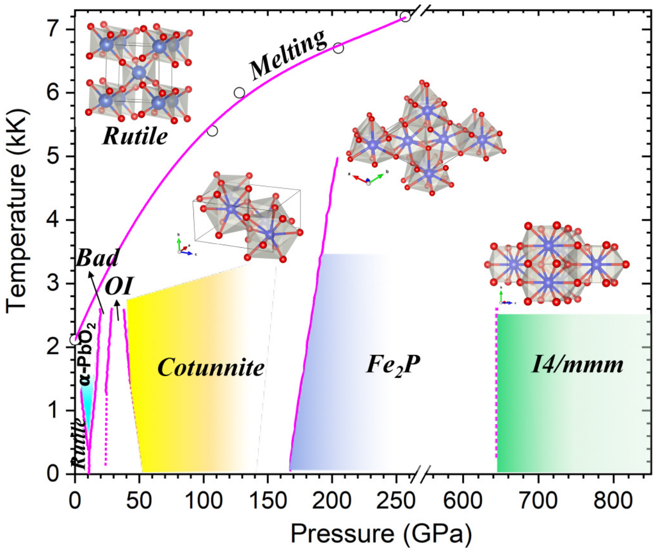

FIG. 1. Phase diagram of TiO_2. Inset: Sixfold coordinated rutile, sevenfold coordinated cotunnite, ninefold coordinated Fe_2P and predicted tenfold coordinated *I*4/*mmm* structure. Blue spheres represent Ti cations and red spheres represent oxygen anions. The data for the solid phases in the phase diagram are obtained from previous studies [2–8]. The open circles are the QMD melting points obtained from this study. The phase sequence observed in static experiments are rutile ⇒ α-PbO_2 ⇒ baddeleyite (bad) ⇒ orthorhombic I (OI) ⇒ cotunnite ⇒ Fe_2P.

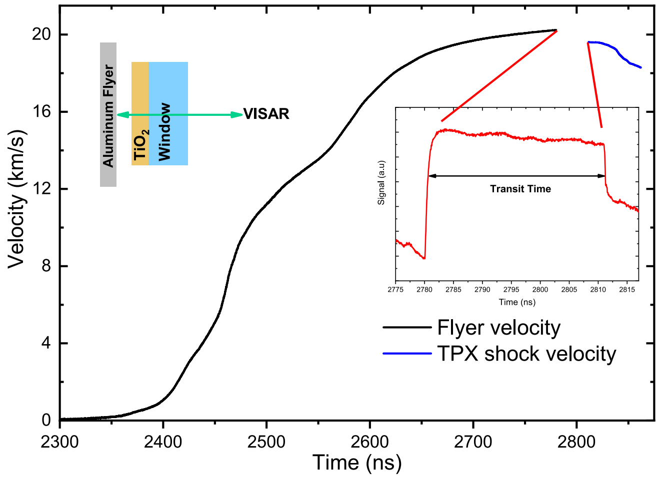

FIG. 2. A typical VISAR trace from a Z experiment showing the aluminum flyer velocity (black) and the shock velocity in the TPX window (blue). The VISAR does not record a velocity signal in the TiO_2. Inset: Raw VISAR signal from the TiO_2 sample showing the transit-time fiducials and a schematic illustration of the Z-experimental setup.

current pulses in excess of 20 MA and magnetic fields of 1000 T over a few hundred ns [22]. The combined current and magnetic field generate a Lorentz force ($F = J \times B$) that can accelerate aluminum flyer plates up to 40 km/s. We optimize current pulses to shocklessly accelerate the flyer plates to a terminal velocity and ensure that the impact side of the flyer plate remains at solid density [23–25]. The Z flyer-plate technique produces precision Hugoniot data consistent with gas-gun, high explosive, and nuclear-driven shock compression methods and has been used to examine the high pressure response of a variety of materials [21,26–29].

The TiO_2 rutile single crystals oriented [100], [110], and [001] (Asphera and MTI Corporation) were cut and polished into 5-mm squares with thicknesses of approximately 0.5 mm with an uncertainty of 3–5 μm. We used an initial density of 4.25 g/cm^3 with an uncertainty of 0.3%. The TiO_2 samples were backed by either poly (4-methyl-1-pentene) plastic, commonly known as TPX, or quartz windows (see Fig. 2) to examine release paths from the Hugoniot state.

A velocity interferometer system for any reflector (VISAR) [30] was the primary diagnostic. Since all materials were transparent, the VISAR laser (532 nm) passed through the TiO_2/window stack and reflected off the flyer-plate surface; the flyer velocity was tracked from launch up to impact with the sample. Figure 2 shows a VISAR trace from an experiment with TPX as the window material. The black line corresponds to the flyer velocity profile and blue trace corresponds to the shock velocity in the TPX window. In this experiment, the flyer reached a velocity of 20 km/s at impact and the resulting shock in TiO_2 was not reflective. We determined the TiO_2 shock velocity from the shock transit time (Fig. 2 inset) and sample thickness, whereas the shock velocity in the window (TPX or quartz) was directly measured from the reflecting shock front. At the highest pressures, the Z-VISAR did detect reflectivity of the shock front, however, the signal was weak and noisy, so transit time analysis was used. We monitored the shock velocity in a quartz witness window to monitor shock velocity acceleration and to provide a correction to the TiO_2 transit-time-calculated shock velocity. Multiple velocity sensitivities, measured in velocity per fringe (VPF), were used to resolve ambiguity in the shock velocity. The window correction for reflective shock fronts is the ambient index of refraction [27], which for TPX and quartz is 1.461 [31] and 1.547 [27], respectively.

From the directly measured flyer velocities and the shock velocities, we determine the final Hugoniot state using Monte Carlo impedance matching (MCIM) [32] and the Hugoniot jump conditions [33] for conservation of mass and momentum,

$$P = P_0 + \rho_0 U_S U_P, \tag{1}$$

$$\rho = \frac{\rho_0 U_S}{U_S - U_P}, \tag{2}$$

where ρ is density, P is pressure, U_S is shock velocity, and U_P is particle velocity. The subscript 0 denotes the initial states. The MCIM technique process uses 1 000 000 iterations and computes the final Hugoniot state. Table I [31] and Table II [27] lists the linear fit parameters and the off-diagonal term in the covariance matrix for the aluminum flyer plate, quartz, and TPX back windows. Tables III and VI list the MCIM-determined principal Hugoniot data and release state data, respectively.

TABLE I. Linear fit parameters to $U_S = C_0 + S_1 U_P$ and the off-diagonal term in the covariance matrix used in Monte Carlo method.

Material	C_0 (km/s)	S_1 (km/s)	$\sigma_{C_0 S_1} \times 10^3$
Aluminum	6.322 ± 0.231	1.188 ± 0.020	-4.605
TPX	1.984 ± 0.134	1.357 ± 0.009	-1.221
TiO_2	5.32 ± 0.10	1.34 ± 0.01	-7.500

III. OMEGA—EXPERIMENTAL METHODS

While the Z Hugoniot data provide valuable information on density and pressure at extreme conditions, the data are not enough to generate a complete EOS because they lack information on temperature. To complement the high-precision Z Hugoniot data, we conducted temperature measurements along the TiO_2 Hugoniot using decaying shock experiments at the Omega EP [34] and Omega [35] laser facilities located at the University of Rochester's Laboratory for Laser Energetics.

Figure 3 shows a schematic view of the Omega decaying shock experiments. The targets consisted of 50-μm-thick layers of polyimide (Dupont Kapton) and oxygen free high thermal conductivity copper, backed by adjacent 500-μm-thick quartz and TiO_2 [100] crystal samples. The back surfaces of the quartz and TiO_2 samples had an antireflective coating to minimize Fresnel reflections. Lateral dimensions of the polyimide and copper layers were 4-mm square. The polyimide is a low-Z ablator that efficiently absorbs the UV laser and drives a shock through the copper layer and into the quartz and TiO_2. The 50-μm-thick copper layer was sufficiently thick to absorb all x rays and hot electrons produced through laser-plasma interactions in the ablator and to eliminate any measurable preheat in the samples. Laser intensities ranged from 0.5 to $1.0 \times 10^{14}\ \mathrm{W/cm^2}$ and the drive laser spot sizes were 1.8-mm diameter for Omega EP, and 800-μm diameter for Omega with temporally square pulses 2-3 ns in duration. The copper thickness allowed for the rarefaction wave from the ablation front to overtake the shock front immediately prior to breaking out of the copper, thus maximizing the amount of decaying shock observed within the streak window.

At high shock pressures and temperatures, both the quartz and TiO_2 melt into metallic fluids, which produces a reflective shock front. A line-imaging VISAR [36] measured the shock velocity of the front as it transits through the samples. Figure 3 shows a typical line-VISAR image and shock velocity profiles from TiO_2 [100] and quartz during the decaying shock experiment. Time-dependent fringe intensity provides information about the reflectivity as a function of the shock velocity. The quartz and TiO_2 samples are normalized to the reflectivity of the copper baseplate to eliminate spatial variation in the VISAR probe laser. The VISAR uses dual VPFs to eliminate 2π ambiguities in phase. We analyzed the line-VISAR data using the Fourier transform method [37]. The VPF correction for reflective shock fronts are 1.547 for quartz and 2.668 for TiO_2 [100] [38]. The velocity uncertainty is approximately 3% of a fringe.

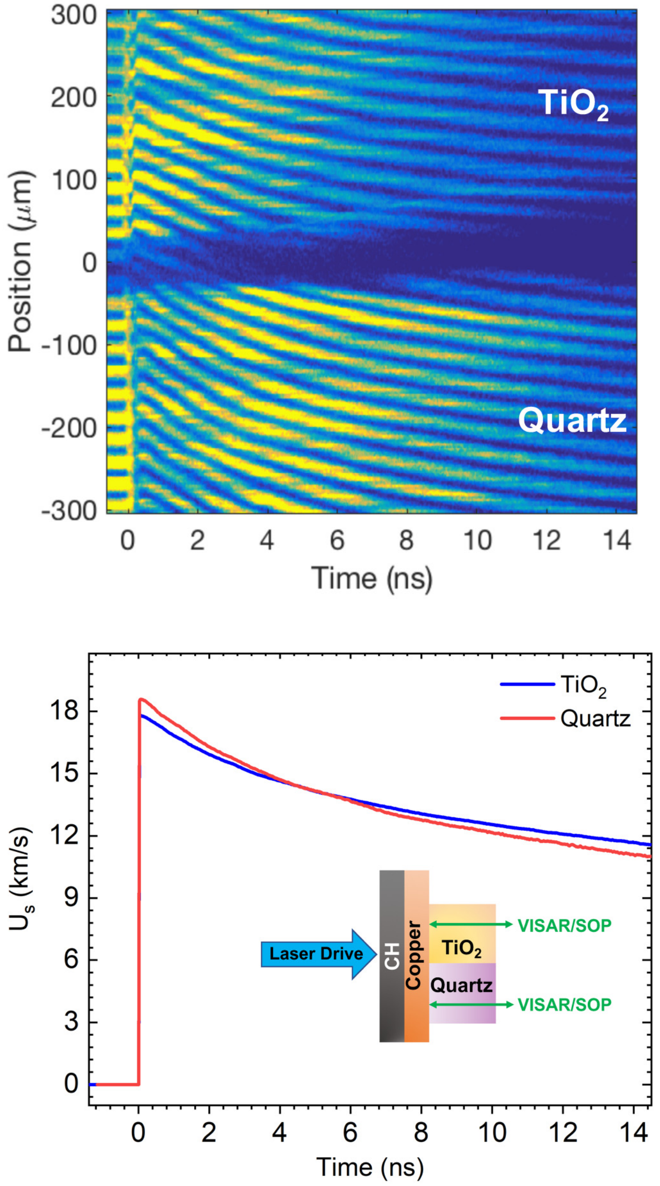

FIG. 3. Top: Representative data from the Omega line-VISAR imaging system. Bottom: Analyzed line-VISAR data showing the TiO_2 and quartz shock velocities as a function of time. Inset: Experimental setup for laser experiments.

To determine temperature along the decaying shock, a streaked optical pyrometer (SOP) [39] measured the optical emission from the shock front over the wavelength range 590 to 850 nm. Figure 4 shows a representative data image from the SOP. Combining the SOP data with the line-VISAR result

TABLE II. Parameters for the cubic fit $U_S = C_0 + C_1 U_P + C_2 U_P^2 + C_3 U_P^3$ to the quartz Hugoniot data.

C_0 (km/s)	C_1 (km/s)$^{-1}$	C_2 (km/s)$^{-2}$	C_3 (km/s)$^{-3}$
1.754 ± 0.412	1.862 ± 0.135	$(-3.364 \pm 1.33) \times 10^{-2}$	$(5.666 \pm 0.04) \times 10^{-4}$

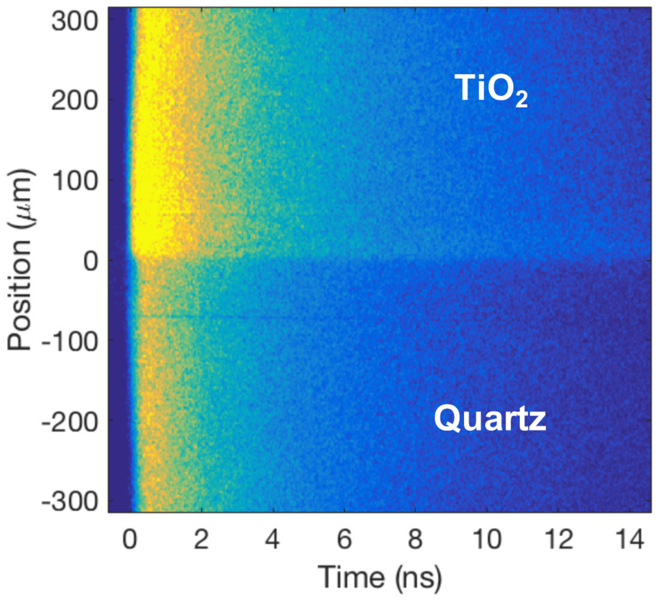

FIG. 4. Typical representative of the SOP data from TiO_2 (top half) and quartz (bottom half).

provides the shock front emission as a function of velocity (and hence pressure). The Omega VISAR/SOP telescope had recently been upgraded at the time of these experiments and an absolute calibration had not yet been performed, so we performed a relative calibration for the SOP using the adjacent quartz samples and the previously measured temperature along the quartz Hugoniot [11,37]. We adapted a gray-body approximation using the shock-front reflectivity from line-VISAR and emission from SOP to determine the temperature in the TiO_2 samples. Temperature uncertainty is estimated to be 10–15% from the relative calibration, TiO_2 reflectivity, and measured emission.

IV. QUANTUM MOLECULAR DYNAMICS SIMULATIONS

The results from the Z and Omega experiments provide valuable EOS data at a continuum level. To further explore the TiO_2 system at extreme conditions, we conducted DFT-based molecular dynamics (QMD) simulations using spin-polarized DFT with Mermin's generalization to finite temperature [41], as implemented in the Vienna an initio simulation package [42,43] (VASP, v. 5.3.5). We used the generalized gradient approximation [44], with the Perdew, Burke, and Ernzerhof (PBE) [45] parametrization for the exchange-correlation energy.

The projector augmented-wave (PAW) method [46,47] describes the interaction between the valence electrons and the ionic cores. The Ti (*3d, 4s*) and O (*2s, 2p*) electrons are treated explicitly as valence states in the Mermin-Kohn-Sham equations, and, the remaining core electrons together with the nuclei are represented by PAW pseudopotentials. For Ti, we used the PAW PBE, 08Apr2002 and for O we used PAW PBE O_GW, 28Sep2005. The plane-wave cutoff energy for the electronic wave functions was 800 eV, with partial occupan-

TABLE III. Experimentally determined Hugoniot states of TiO_2. The flyer velocity (V_F) and shock velocity (U_S) are directly measured in the experiment. Particle velocity (U_P) and density (ρ), pressure (P) are determined from the Hugoniot jump conditions and Monte Carlo impedance matching technique. The initial density was 4.25 g/cm^3 with an uncertainty of 0.3%.

Shot	Orientation	Window	V_F (km/s)	U_P (km/s)	U_S (km/s)	ρ (g/cm^3)	P (GPa)
Z3297S6[c]	[100]	TPX	22.49 ± 0.09	9.66 ± 0.07	18.24 ± 0.20	9.03 ± 0.11	748.8 ± 6.3
Z3297N6[c]	[100]	TPX	21.10 ± 0.06	9.06 ± 0.05	17.43 ± 0.15	8.85 ± 0.13	671.3 ± 4.4
Z3267S5[c]	[100]	TPX	20.24 ± 0.06	8.72 ± 0.06	16.83 ± 0.18	8.82 ± 0.15	623.5 ± 4.7
Z3267N5[c]	[100]	TPX	18.77 ± 0.06	8.10 ± 0.05	15.90 ± 0.15	8.67 ± 0.13	547.7 ± 3.9
Z3343N6	[100]	TPX	16.52 ± 0.09	7.08 ± 0.06	14.86 ± 0.18	8.12 ± 0.14	447.3 ± 4.5
Z3274S5	[100]	TPX	14.74 ± 0.06	6.34 ± 0.05	13.71 ± 0.18	7.91 ± 0.14	369.8 ± 3.5
Z3274N5	[100]	TPX	13.59 ± 0.06	6.35 ± 0.05	13.18 ± 0.14	7.62 ± 0.10	326.3 ± 2.8
Z3325N1[a]	[100]	TPX	12.83 ± 0.09	5.44 ± 0.03	12.79 ± 0.15	7.39 ± 0.11	295.2 ± 3.4
Z3427N5	[100]	TPX	10.94 ± 0.05	4.71 ± 0.05	11.55 ± 0.18	7.18 ± 0.12	231.2 ± 2.5
Z3441S7	[100]	Quartz	24.27 ± 0.09	10.40 ± 0.08	19.34 ± 0.26	9.19 ± 0.22	854.9 ± 8.0
Z3343N7	[100]	Quartz	16.52 ± 0.14	7.07 ± 0.09	14.91 ± 0.26	8.08 ± 0.18	448.2 ± 6.2
Z3391S2	[100]	Quartz	13.51 ± 0.06	5.80 ± 0.05	13.08 ± 0.14	7.64 ± 0.10	322.5 ± 2.8
Z3325N5[b]	[100]	Quartz	12.77 ± 0.07	5.47 ± 0.05	12.67 ± 0.06	7.48 ± 0.10	294.5 ± 3.0
Z3396S3	[100]	Quartz	11.56 ± 0.05	4.97 ± 0.05	11.93 ± 0.19	7.29 ± 0.13	252.0 ± 2.7
Z3441N7	[110]	TPX	22.68 ± 0.07	9.75 ± 0.07	18.30 ± 0.25	9.09 ± 0.21	758.2 ± 6.9
Z3343S3	[110]	TPX	17.81 ± 0.09	7.64 ± 0.06	15.59 ± 0.14	8.33 ± 0.12	506.1 ± 4.3
Z3391N5	[110]	TPX	13.15 ± 0.15	5.84 ± 0.05	13.15 ± 0.15	7.64 ± 0.11	326.2 ± 2.9
Z3396N5	[110]	TPX	11.74 ± 0.08	5.04 ± 0.05	12.08 ± 0.15	7.29 ± 0.11	258.7 ± 3.0
Z3391N2	[001]	TPX	13.56 ± 0.08	5.82 ± 0.06	13.14 ± 0.19	7.63 ± 0.14	325.0 ± 3.7
Z3396N2	[001]	TPX	11.70 ± 0.07	5.06 ± 0.05	11.85 ± 0.15	7.42 ± 0.11	254.9 ± 2.8

[a] A shock formed in the aluminum flyer so the density was corrected to 2.64 g/cm^3 with an uncertainty of 1%.

[b] A shock formed in the aluminum flyer so the density was corrected to 2.69 g/cm^3 with an uncertainty of 1%.

[c] The Z VISAR detected weak reflectivity, but transit time analysis was used due to noise in the signal.

TABLE IV. The QMD calculated Hugoniot states for the three TiO_2 polymorphs.

Form	ρ (g/cm^3)	P (GPa)	T (K)	U_P (km/s)	U_S (km/s)
Rutile	6.44	152.51	4000	3.38	9.88
$\rho_0 = 4.233$ g/cm^3	6.49	165.69	5000	3.56	10.25
$P_0 = 10.96$ GPa	7.14	262.64	6000	4.92	12.08
	7.49	334.83	8000	5.76	13.26
	7.85	406.60	10 000	6.56	14.24
	8.97	684.25	20 000	9.16	17.35
	9.60	900.85	30 000	10.84	19.39
	10.09	1108.98	40 000	12.27	21.14
	10.46	1309.12	50 000	13.51	22.69
	10.87	1513.27	60 000	14.72	24.11
	11.14	1723.63	70 000	15.84	25.54
	11.43	1942.34	80 000	16.95	26.92
	11.63	2164.26	90 000	17.98	28.28
	11.92	2393.41	100 000	19.05	29.54
Anatase	7.02	267.82	8000	5.45	12.22
$\rho_0 = 3.89$ g/cm^3	7.32	329.39	10 000	6.22	13.27
$P_0 = 8.59$ GPa	8.34	570.30	20 000	8.78	16.45
	8.99	770.98	30 000	10.54	18.58
	9.38	953.20	40 000	11.92	20.37
	9.80	1138.79	50 000	13.24	21.95
	10.13	1320.13	60 000	14.41	23.39
	10.35	1517.95	70 000	15.56	24.93
	10.68	1712.73	80 000	16.69	26.25
	10.85	1916.18	90 000	17.73	27.65
	11.17	2124.89	100 000	18.83	28.89
Brookite	7.35	315.12	8000	5.69	12.99
$\rho_0 = 4.13$ g/cm^3	7.69	383.61	10 000	6.47	13.98
$P_0 = 9.56$ GPa	8.78	649.66	20 000	9.06	17.11
	9.41	861.65	30 000	10.76	19.17
	9.89	1062.79	40 000	12.18	20.92
	10.28	1258.27	50 000	13.44	22.48
	10.64	1454.63	60 000	14.63	23.91
	10.91	1662.18	70000	15.76	25.37
	11.21	1874.10	80000	16.88	26.74
	11.39	2089.46	90000	17.91	28.10
	11.69	2312.06	100000	18.98	29.36

cies for all bands controlled by Fermi-Dirac smearing, and we imposed stringent convergence settings, which are necessary to analyze high-pressure experiments [48].

The simulations used a 3D-periodic 2 × 2 × 2 supercell including 48 atoms (16 f.u.) to ensure that the interaction of molecular structures with their periodic images is negligible. Baldereschi's mean-value special k point [49] was used for properties averaging in the Brillouin zone. We set the time step for ion motion to 0.7 fs, with velocities scaled to the temperature at each simulation step, and each simulation ran for $\sim 3-8$ ps. Equilibration was achieved when the block average [50] of the standard deviation of the pressure was less than 0.5%.

We sampled the phase space by running canonical-ensemble QMD simulations with fixed number of particles, volume, and temperature. We calculated isotherms on liquid TiO_2 between 4 000 and 100 000 K and densities from 2 to 20 g/cm^3 in increments of 1 g/cm^3. This grid spacing balances between errors introduced by birational interpolation and QMD computational time to generate each (P, T) point. To determine the principal Hugoniot state for each specific volume, we interpolate between the two (P, T) points that bracket the Hugoniot temperature and pressure and solve for the Hugoniot energy equation,

$$E - E_0 + 1/2(P + P_0)(V - V_0) = 0, \tag{3}$$

where E is the specific internal energy, P is the pressure, $V = 1/\rho$ is the specific volume of shocked TiO_2 bulk, and E_0 and P_0 are the reference energy and pressure determined from QMD simulations at 300 K. The reference structure for the Hugoniot was the synthetic rutile-type TiO_2 bulk structure (space group $P4_2/mnm$, IT No. 136; $Z = 2$) observed experimentally under ambient conditions [51], with equilibrium lattice parameters $a_0 = 4.5922(2)$ Å, $c_0 = 2.9574(2)$ Å, corresponding to an initial volume per atom of $V_0 = 10.394$ Å and a density of $\rho_0 = 4.233$ g/cm^3. The calculated reference energy and pressure were $E_0 = -8.682$ eV/atom and $P_0 = 10.96$ GPa, respectively. This computational approach has successfully predicted the EOS for numerous metals and oxides subjected to high pressure and high temperature [21,28,48,52–54].

For completeness, we performed additional Hugoniot calculations for brookite [55] ($\rho_0 = 4.13$ g/cm^3) and anatase [56] ($\rho_0 = 3.89$ g/cm^3) phases of TiO_2. The computed reference energy and pressure at 300 K were $E_0 = -8.718$ eV/atom and $P_0 = 9.56$ GPa for brookite and $E_0 = -8.736$ eV/atom and $P_0 = 8.59$ GPa for anatase. Table IV lists the calculated Hugoniot states for the three TiO_2 polymorphs.

In addition, we determined the melting curves of the high-pressure cotunnite-type and Fe_2P-type phases of TiO_2 from QMD simulations using the hysteresis method [57]. In the simulations, the cotunnite $PbCl_2$-structured phase [51] (space group $Pnma$, IT No. 62; $Z = 4$) used a 192-atom 2 × 4 × 2 supercell and the Fe_2P type phase[2] (space group $P\bar{6}2/m$, IT No. 189; $Z = 3$) used a 243-atom 3 × 3 × 3 supercell. These melting points are presented in Figs. 1 and 10 as circles. A solid line is used as a guide to connect the ambient melting point of 2128 K [58] with the QMD melting data.

V. RESULTS AND DISCUSSION

Figure 5 shows the Hugoniot data in the $U_s - U_p$ plane from the current Z experiments, the QMD simulations, and the prior data [13–17]. An enlarged version focusing on the lower pressure region is shown in Fig. 6. The Z data show a linear trend with no slope changes over the range we explored. The QMD calculations are in good agreement with the Z data. We observe no crystal orientation dependence in the data; the [100], [110], and [001] data are consistent with each other. We calculated two fits to the data. The first fit is a weighted linear fit to the Z data only: $U_S = C_0 + S_1 U_P$. Table I lists the fit parameters and off-diagonal value of the covariance matrix. For extrapolating to higher pressures, we fit the combined Z data and QMD data using a modified version of the universal

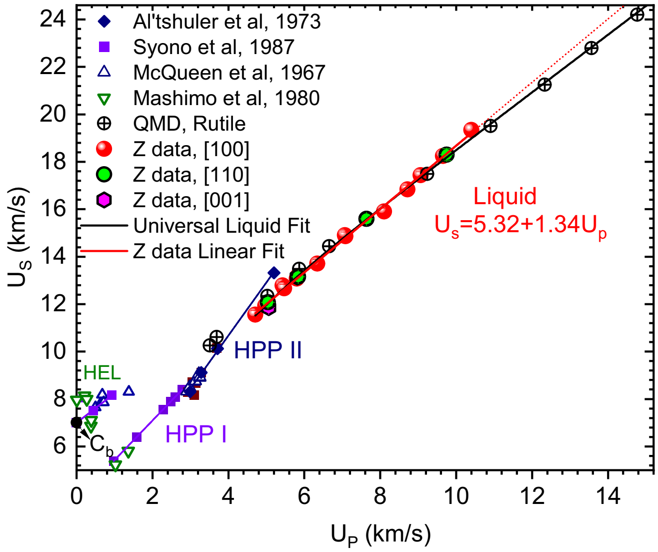

FIG. 5. TiO_2 Hugoniot in the $U_s - U_p$ plane, including data from the current Z experiments, QMD simulations, and the previous Hugoniot data for [100] orientation [13–17]. The error bars lie within the symbols.

liquid Hugoniot [27,59]:

$$U_S = A + BU_P - CU_P \exp(-DU_P). \tag{4}$$

This functional form asymptotically approaches a linear $U_S - U_P$ relation for a wide range of U_P. The QMD data were assumed to have 5% uncertainty, so the experimental data were weighted more heavily. The results for this fit are listed in Table V. The linear fit is valid from U_p of 4.7 to 10.5 km/s. Although the highest Z-Hugoniot point and QMD appear to deviate (however, within the error bar), we note the deviation is likely caused by experimental scatter. The deviation of the two fits also suggests that the TiO_2 Hugoniot begins to display some curvature, similar to what has been observed for SiO_2 [27,29].

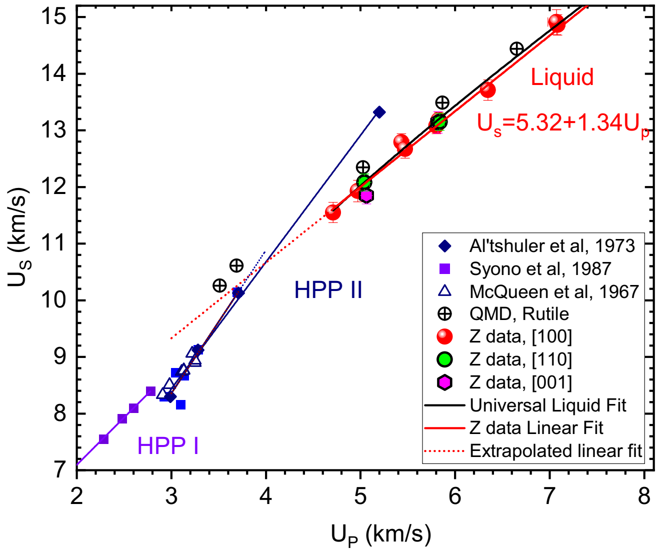

FIG. 6. Enlarged TiO_2 Hugoniot in the $U_s - U_p$ plane, including data from the current Z experiments, QMD simulations, and the previous Hugoniot data for [100] orientation [13–17]. The dotted lines are extrapolated linear fits.

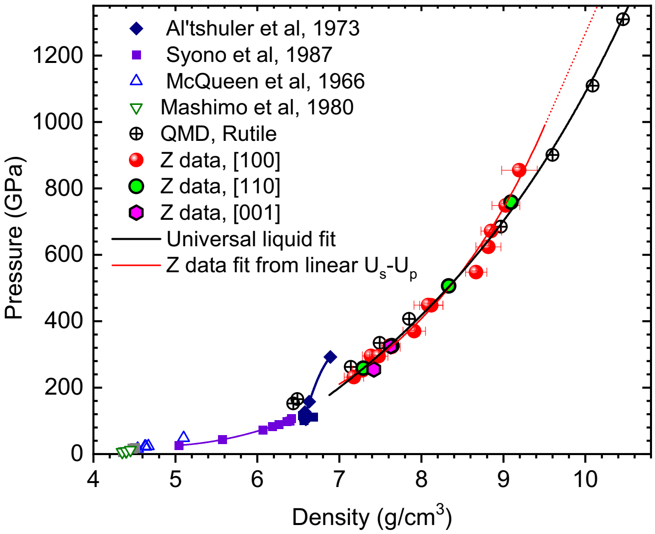

FIG. 7. TiO_2 Hugoniot in the $P - \rho$ plane, including data from the current Z experiments, QMD simulations, and the previous Hugoniot data for [100] orientation [13–17]. The error bars lie within the symbols if not shown in the plot.

Figure 7 plots the combined Hugoniot data in the $P - \rho$ plane. Even though the $P - \rho$ plane is more sensitive to changes in U_S, the data show no dependence on the crystal orientation. The Z data monotonically increase in density with increasing pressure up to a maximum pressure of 855 GPa and compression of 2.16. Again, we see good agreement between the Z data and QMD calculations over the common range. Although the highest pressure Z point and QMD appear to deviate, it is still within the uncertainty of experimental data.

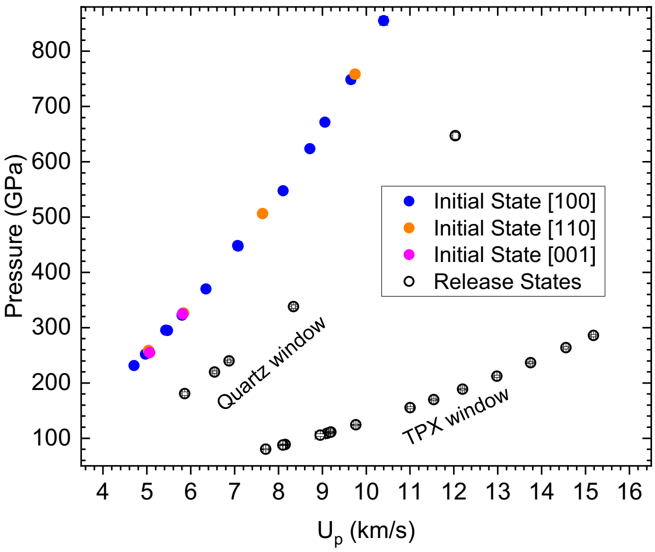

FIG. 8. $P - U_P$ plot showing the initial Hugoniot states and the corresponding release states calculated from Monte Carlo impedance matching method.

TABLE V. The modified, universal liquid fit $U_S = A + BU_P - CU_P \exp(-DU_P)$ parameters to the TiO_2 Hugoniot.

A (km/s)	B	C	D (km/s)$^{-1}$
6.375 ± 0.211	1.213 ± 0.014	6.742 ± 0.793	0.855 ± 0.376

Further data at higher pressures would resolve the discrepancy.

Prior work by Al'tshuler *et al.* [14] and Syono [17] proposed a phase transformation from HPP-I to HPP-II (HPP = high pressure phase) at $U_S = 8.2$ km/s and 107 GPa, based on the discontinuity in the $U_s - U_p$ slope. The proposed HPP-II phase was nearly incompressible with a maximum compression of 1.6 as shown in Fig. 7. Contrary to the Al'tshuler *et al.* data, our recent Z data show a more compressible Hugoniot above the U_S of 11 km/s. Differences between this work and the Al'tshuler *et al.* work are that they used randomly oriented, natural TiO_2 crystals with initial densities of 4.21 g/cm^3, which is lower than the synthetically grown single crystals ($\rho_0 = 4.25$ g/cm^3). The results from McQueen [13] and Syono [17] indicate that these differences have little affect on the Hugoniot above 80 GPa. More interestingly, in the same paper, Al'tshuler *et al.* also reported CaF_2 becomes highly incompressible above 100 GPa. However, recent studies by Root *et al.* [19] and Shu *et al.* [20] show that CaF_2 is not incompressible. This suggests the possibility of a systematic experimental error in their studies, although we note that the Al'tshuler *et al.* data did not list error bars. Our results clearly indicate that TiO_2 is not incompressible, at least up to 855 GPa.

Figure 8 shows the release states of TiO_2 into the TPX/quartz windows, together with the initial state. The release data provide an additional constraint for the development of an EOS. The experiments that had quartz or TPX as windows are labeled accordingly next to the release states. The release states from quartz are higher than those obtained from TPX, due to the high impedance of quartz. Because of acceleration, we use the linear fit in Table I and the acceleration corrected shock velocity, $U_{S\text{prior}}$ in Table VI, to determine the initial shock state prior to shock transit into the window. We observed a uniform increase in particle velocity, with increase in pressure for the initial and release states.

Figure 9 shows the Hugoniot temperature as a function of the experimentally measured shock velocity from the decaying shock, laser-driven Omega experiments. The temperature ranged from ∼52 000 K to ∼5000 K with corresponding shock velocities from 24 km/s to 10.9 km/s. Over this range, the liquid state QMD simulations are in good agreement with the experimental data. In decaying shocks, usually an inflection point or plateau in the pyrometry data points to a phase transition [60]. The data show that the shock temperature increases monotonically with increasing shock velocity and pressure, suggesting the data in the decaying shock experiments correspond to the same phase with no phase transitions.

The inset in Fig. 9 shows the reflectivity as a function of shock velocity. A significant increase in reflectivity is observed with increasing shock velocity. At pressures below 230 GPa ($U_s = 12$ km/s), the reflectivity is only about a few percent, most likely due to the onset of melting. As the shock velocity (and shock pressure) increases above 12 km/s, the reflectivity rapidly increases until about 450 GPa ($U_S = 15$ km/s) where the reflectivity begins to plateau. This rapid increase in reflectivity is likely from the dissociation into an atomic fluid. Similar behavior of change in the reflectivity has previously been reported for the structural analog, SiO_2, which have been attributed to a continuous dissociation of a molecular system [40,61]. We do not observe any anomalous

TABLE VI. Reshock states of TiO_2 calculated using Monte Carlo method.

Shot	Orientation	Window	U_S^{window} (km/s)	$U_{S\text{prior}}$ (km/s)	U_{P2} (km/s)	ρ_2 (g/cm^3)	P_2 (GPa)
Z3297S6	[100]	TPX	21.74 ± 0.06	18.36 ± 0.20	14.56 ± 0.05	6.85 ± 0.25	263.6 ± 2.1
Z3297N6	[100]	TPX	20.65 ± 0.04	17.61 ± 0.14	13.75 ± 0.04	6.69 ± 0.18	236.6 ± 1.6
Z3267S5	[100]	TPX	19.6 ± 0.07	16.85 ± 0.18	12.98 ± 0.06	6.50 ± 0.24	211.9 ± 1.9
Z3267N5	[100]	TPX	18.54 ± 0.04	15.96 ± 0.15	12.20 ± 0.04	6.12 ± 0.21	188.4 ± 1.3
Z3343N6	[100]	TPX	16.92 ± 0.08	15.06 ± 0.18	11.01 ± 0.07	5.77 ± 0.26	155.1 ± 1.8
Z3274S5	[100]	TPX	15.24 ± 0.04	13.85 ± 0.18	9.77 ± 0.05	5.57 ± 0.27	124.0 ± 1.0
Z3274N5	[100]	TPX	14.35 ± 0.05	13.18 ± 0.14	9.11 ± 0.06	5.52 ± 0.22	108.9 ± 1.1
Z3325N1	[100]	TPX	14.14 ± 0.15	12.83 ± 0.18	8.95 ± 0.12	5.17 ± 0.31	105.5 ± 2.5
Z3427N5	[100]	TPX	12.45 ± 0.05	11.63 ± 0.18	7.71 ± 0.06	4.73 ± 0.31	79.9 ± 0.9
Z3441S7	[100]	Quartz	20.28 ± 0.08	19.44 ± 0.26	12.03 ± 0.06	9.27 ± 0.32	646.9 ± 5.9
Z3343N7	[100]	Quartz	15.28 ± 0.06	15.09 ± 0.22	8.34 ± 0.04	7.88 ± 0.33	337.9 ± 3.1
Z3391S2	[100]	Quartz	13.15 ± 0.05	13.22 ± 0.14	6.87 ± 0.03	7.01 ± 0.28	239.6 ± 2.1
Z3325N5	[100]	Quartz	12.66 ± 0.06	12.71 ± 0.16	6.55 ± 0.04	6.63 ± 0.38	219.6 ± 2.4
Z3396S3	[100]	Quartz	11.63 ± 0.09	11.97 ± 0.19	5.86 ± 0.06	6.42 ± 0.45	180.7 ± 3.2
Z3441N7	[110]	TPX	22.59 ± 0.06	18.58 ± 0.25	15.18 ± 0.05	6.52 ± 0.31	285.7 ± 2.2
Z3343S3	[110]	TPX	17.65 ± 0.05	15.71 ± 0.14	11.54 ± 0.05	6.45 ± 0.20	169.7 ± 1.4
Z3391N5	[110]	TPX	14.47 ± 0.05	13.29 ± 0.15	9.20 ± 0.06	5.58 ± 0.23	110.9 ± 1.1
Z3396N5	[110]	TPX	13.05 ± 0.05	12.12 ± 0.15	8.15 ± 0.06	4.99 ± 0.25	88.6 ± 1.0
Z3391N2	[001]	TPX	14.45 ± 0.05	13.28 ± 0.19	9.18 ± 0.05	5.58 ± 0.29	110.6 ± 1.1
Z3396N2	[001]	TPX	12.98 ± 0.06	11.89 ± 0.15	8.10 ± 0.06	4.69 ± 0.26	87.6 ± 1.1

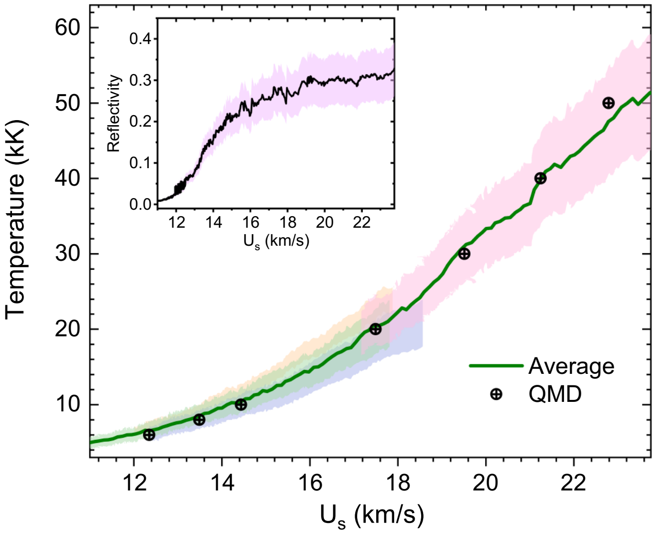

FIG. 9. Experimental shock temperature versus shock velocity compared with QMD. The shaded area represents the error on the experimental data. The green line is the average of four different experiments. Note that each color corresponds to a separate experiment. Inset: Reflectivity data as a function of shock velocity.

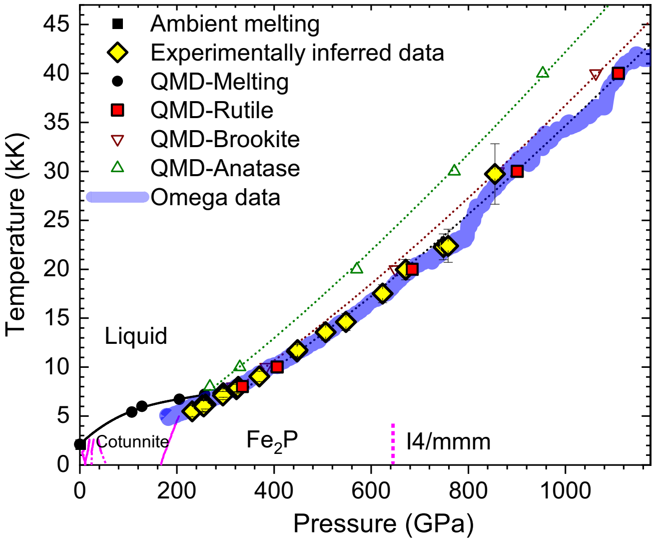

FIG. 10. Phase diagram of TiO_2 with experimental $P-T$ points and the QMD calculated melt line. The diamond symbols are experimentally inferred $P-T$ points combining the temperature data from the Omega laser shock data and the pressure data from the Z experiments. The magenta lines for the solid phase are obtained from previous studies [2,7,8,62]. The violet line is the converted Omega data from U_s-T to $P-T$ using the modified U_s-U_p universal liquid fit.

behavior in the reflectivity that would indicate a phase transition.

To gain insight into where melting could possibly occur, we performed a linear fitting for the Al'tshuler data (Fig. 6), excluding their highest-pressure data. The linear fit extrapolation for the HPPII (without the highest-pressure data) and the Z-based liquid fit intersects at $U_p = 3.8$ km/s and $U_s = 10.4$ km/s, which corresponds to a pressure of 170 GPa. The liquid QMD points at 165 and 152 GPa are higher in pressure than the extrapolation of the solid TiO_2 Hugoniot. Although the QMD and the Al'tshuler point at ($U_S = 10$ km/s) are close, the difference between the QMD and the linear fits suggests that TiO_2 is still solid at these pressures or possibly just beginning to melt. The intersection of the Z-data liquid fit and the solid-data fit suggests melting occurs between 165 GPa and 230 GPa.

Furthermore, in SiO_2, melting was observed at 5000 K [40] and 8300 K for stishovite [60] (dense form of SiO_2) as a kink in their shock temperature versus the shock velocity plot. In our current data, we do not observe a kink in the TiO_2 U_s-T data because melting has likely occurred below our data range. Moreover, in SiO_2, melting was observed as a continuous transition from solid to liquid. Another possibility for not observing such a continuous melt in TiO_2 could be the detectable limit for the current SOP at Omega being 4000–4500 K. From our results and the extrapolation of Al'tshuler's data in Fig. 6, we speculate the melting to occur below 4000 K, which is below the range of the SOP.

We posit that all the Z-TiO_2 data in this study are in a liquid phase based on the following: (i) no crystal orientational dependence in the Hugoniot data above 230 GPa, (ii) increase in reflectivity starting at U_S of 12 km/s (reflectivity usually suggests melting [27]), (iii) the good agreement between the QMD liquid-state Hugoniot simulations and the experimental data, and (iv) the change in slope between the extrapolated solid line for HPPII and liquid fit. The onset and completion of melt most likely occurs between 165 and 230 GPa. However, determining the exact location of the melt transition on the Hugoniot will require further studies, such as sound speed measurements, in the 100 GPa to 230 GPa range.

Figure 10 replots the phase diagram of TiO_2 together with the experimentally inferred $P-T$ Z-data and the U_S-T decaying shock data converted to $P-T$ (violet band in Fig. 10) using the modified universal liquid fit in Eq. (4). For completeness, we include the QMD Hugoniot calculations for the brookite and anatase phases. Both phases show the same trend as rutile with shifted behavior due to the difference in the initial state density. All three forms are in liquid phase over this range.

The QMD melt line predicted in this study is 1000 K higher than the experimental data, which are already likely in a liquid phase. One possible reason for this discrepancy could be that the supercell sizes used in the grid calculations for the liquid state are smaller than the ones used in the melting curve calculations. This could have some impact on the melting curve position in both sets of calculations. It is also possible that a high-pressure, high-temperature phase exists and that melt does not initiate from the cotunnite or Fe_2P phase. Further QMD and experimental work are needed to more accurately determine the melt boundary.

VI. SUMMARY

We present high-precision experimental Hugoniot data in pressure and temperature for TiO_2 at pressure ranges from 230 to 855 GPa – a previously unexplored regime using the Sandia Z-machine and Omega laser facility. Our data show a strikingly different behavior for TiO_2 than that proposed previously by Al'tshuler *et al.* [14] Our Z data combined with Omega and QMD data confirm that TiO_2 is at a liquid state above 230 GPa. Moreover, the excellent agreement of the experimental and QMD data further establishes the validity of the QMD work. These high-pressure data on TiO_2 will enable us to constrain the EOS, which can be used to investigate the relevant material properties. In addition, this high-pressure data on TiO_2 is of significant importance, owing to the fact that TiO_2 is a molecular analog of SiO_2. With the discovery of super-Earths and extrasolar giant planets, studying TiO_2 provides a reference on how SiO_2 could behave at those extreme pressures that are hard to achieve routinely in a laboratory.

ACKNOWLEDGMENTS

We would like to thank the large Z team at Sandia and Omega operation staff for their invaluable efforts during the experiment. Sandia National Laboratories is a multimission laboratory managed and operated by National Technology and Engineering Solutions of Sandia, LLC, a wholly owned subsidiary of Honeywell International Inc., for the US Department of Energy's National Nuclear Security Administration under Contract No. DE-NA0003525. This paper describes objective technical results and analysis. Any subjective views or opinions that might be expressed in the paper do not necessarily represent the views of the US Department of Energy or the United States Government.

---

[1] A. R. Albuquerque, J. Maul, E. Longo, I. M. G. Dos Santos, and J. R. Sambrano, J. Phys. Chem. C **117**, 7050 (2013).

[2] H. Dekura, T. Tsuchiya, Y. Kuwayama, and J. Tsuchiya, Phys. Rev. Lett. **107**, 045701 (2011).

[3] L. Gerward and J. S. Olsen, J. Appl. Crystallogr. **30**, 259 (1997).

[4] J. S. Olsen, L. Gerward, and J. Z. Jiang, J. Phys. Chem. Solids **60**, 229 (1999).

[5] A. El Goresy, M. Chen, P. Gillet, L. Dubrovinsky, G. Graup, and R. Ahuja, Earth Planet. Sci. Lett. **192**, 485 (2001).

[6] L. S. Dubrovinsky, N. A. Dubrovinskaia, V. Swamy, J. Muscat, N. M. Harrison, R. Ahuja, B. Holm, and B. Johansson, Nature **410**, 653 (2001).

[7] S. Taizo, J. Phys.: Condens. Matter **14**, 10557 (2002).

[8] Y. Al-Khatatbeh, K. K. M. Lee, and B. Kiefer, Phys. Rev. B **79**, 134114 (2009).

[9] R. K. Linde and P. S. Decarli, J. Chem. Phys. **50**, 319 (1969).

[10] M. J. Lyle, C. J. Pickard, and R. J. Needs, Proc. Nat. Acad. Sci. USA **112**, 6898 (2015).

[11] M. Millot, N. Dubrovinskaia, A. Černok, S. Blaha, L. Dubrovinsky, D. G. Braun, P. M. Celliers, G. W. Collins, J. H. Eggert, and R. Jeanloz, Science (New York) **347**, 418 (2015).

[12] F. González-Cataldo, S. Davis, and G. Gutiérrez, Sci. Rep. **6**, 26537 (2016).

[13] R. G. McQueen, J. C. Jamieson, and S. P. Marsh, Science **155**, 1401 (1967).

[14] L. Al'tshuler, M. A. Podurets, G. V. Simakov, and R. F. Trunin, Sov. Phys. Solid State **15**, 969 (1973).

[15] T. Mashimo and A. Sawaoka, Phys. Lett. **78**, 419 (1980).

[16] T. Mashimo, Prof. Mashimo provided updated data on his 1980 publication (private communication).

[17] Y. Syono, K. Kusuba, M. Kikuchi, and K. Fukuoka, *High-Pressure Research in Mineral Physics*, edited by M. H. Manghnani and Y. Syono (Terra/AGU, Tokyo Washington, 1987), pp. 385–392.

[18] W. J. Nellis and T. Petach, in *Shock Compression of Condensed Matter - 2007: Proceedings of the Conference of the American Physical Society Topical Group on Shock Compression of Condensed Matter*, edited by M. Elert, M. D. Furnish, R. Chau, N. Holmes, and J. Nguyen, AIP Conf. Proc. No. 955 (AIP, New York, 2007), p. 89.

[19] S. Root, M. Desjarlais, R. W. Lemke, P. Kalita, and C. S. Alexander, Shock Compression of CaF_2, SAND Report No. SAND2018-0182C, Sandia National Laboratories, 2018.

[20] H. Shu, Y. Zhang, B. Wang, W. Yang, H. Dong, T. Tobase, X. Huang, S. Fu, Q. Zhou, and T. Sekine, Phys. Plasmas **27**, 030701 (2020).

[21] S. Root, J. P. Townsend, E. Davies, R. W. Lemke, D. E. Bliss, D. E. Fratanduono, R. G. Kraus, M. Millot, D. K. Spaulding, L. Shulenburger, S. T. Stewart, and S. B. Jacobsen, Geophys. Res. Lett. **45**, 3865 (2018).

[22] M. E. Savage, L. F. Bennett, D. E. Bliss, W. T. Clark, R. S. Coats, J. M. Elizondo, K. R. LeChien, H. C. Harjes, J. M. Lehr, J. E. Maenchen *et al.*, in *2007 IEEE Pulsed Power Conference*, Vols. 14 (IEEE, Piscataway, New Jersey, 2007), p. 979.

[23] R. W. Lemke, M. D. Knudson, C. A. Hall, T. A. Haill, M. P. Desjarlais, J. R. Asay, and T. A. Mehlhorn, Phys. Plasmas **10**, 1092 (2003).

[24] R. W. Lemke, M. D. Knudson, D. E. Bliss, K. Cochrane, J.-P. Davis, A. A. Giunta, H. C. Harjes, and S. A. Slutz, J. Appl. Phys. **98**, 073530 (2005).

[25] R. W. Lemke, M. D. Knudson, and J.-P. Davis, Int. J. Impact Engng. **38**, 480 (2011).

[26] M. D. Knudson, R. W. Lemke, D. B. Hayes, C. A. Hall, C. Deeney, and J. R. Asay, J. Appl. Phys. **94**, 4420 (2003).

[27] M. D. Knudson and M. P. Desjarlais, Phys. Rev. Lett. **103**, 225501 (2009).

[28] S. Root, L. Shulenburger, R. W. Lemke, D. H. Dolan, T. R. Mattsson, and M. P. Desjarlais, Phys. Rev. Lett. **115**, 198501 (2015).

[29] S. Root, J. P. Townsend, and M. D. Knudson, J. Appl. Phys. **126**, 165901 (2019).

[30] L. M. Barker and R. E. Hollenbach, J. Appl. Phys. **43**, 4669 (1972).

[31] S. Root, T. R. Mattsson, K. Cochrane, R. W. Lemke, M. D. Knudson, S. Root, T. R. Mattsson, K. Cochrane, R. W. Lemke, and M. D. Knudson, J. Appl. Phys. **118**, 205901 (2015).

[32] S. Root, K. R. Cochrane, J. H. Carpenter, and T. R. Mattsson, Phys. Rev. B **87**, 224102 (2013).

[33] G. E. Duvall and R. A. Graham, Rev. Mod. Phys. **49**, 523 (1977).

[34] L. Waxer, D. Maywar, J. Kelly, T. Kessler, B. Kruschwitz, S. Loucks, R. McCrory, D. Meyerhofer, S. Morse, C. Stoeckl, and J. Zuegel, Opt. Photonics News **16**, 30 (2005).

[35] T. Boehly, D. Brown, R. Craxton, R. Keck, J. Knauer, J. Kelly, T. Kessler, S. Kumpan, S. Loucks, S. Letzring, F. Marshall, R.

McCrory, S. Morse, W. Seka, J. Soures, and C. Verdon, Opt. Commun. **133**, 495 (1997).

[36] P. M. Celliers, D. K. Bradley, G. W. Collins, D. G. Hicks, T. R. Boehly, and W. J. Armstrong, Rev. Sci. Instrum. **75**, 4916 (2004).

[37] P. M. Celliers, G. W. Collins, L. B. Da Silva, D. M. Gold, and R. Cauble, Appl. Phys. Lett. **73**, 1320 (1998).

[38] J. R. DeVore, J. Opt. Soc. Am. **41**, 416 (1951).

[39] M. C. Gregor, R. Boni, A. Sorce, J. Kendrick, C. A. McCoy, D. N. Polsin, T. R. Boehly, P. M. Celliers, G. W. Collins, D. E. Fratanduono, J. H. Eggert, and M. Millot, Rev. Sci. Instrum. **87**, 114903 (2016).

[40] D. G. Hicks, T. R. Boehly, J. H. Eggert, J. E. Miller, P. M. Celliers, and G. W. Collins, Phys. Rev. Lett. **97**, 025502 (2006).

[41] N. D. Mermin, Phys. Rev. **137**, A1441 (1965).

[42] G. Kresse and J. Hafner, Phys. Rev. B **47**, 558 (1993).

[43] G. Kresse and J. Furthmüller, Phys. Rev. B **54**, 11169 (1996).

[44] J. P. Perdew, J. A. Chevary, S. H. Vosko, K. A. Jackson, M. R. Pederson, D. J. Singh, and C. Fiolhais, Phys. Rev. B **46**, 6671 (1992).

[45] J. P. Perdew, K. Burke, and M. Ernzerhof, Phys. Rev. Lett. **77**, 3865 (1996).

[46] P. E. Blöchl, Phys. Rev. B **50**, 17953 (1994).

[47] G. Kresse and D. Joubert, Phys. Rev. B **59**, 1758 (1999).

[48] A. E. Mattsson, P. A. Schultz, M. P. Desjarlais, T. R. Mattsson, and K. Leung, Modell. Simul. Mater. Sci. Eng. **13**, R1 (2005).

[49] A. Baldereschi, Phys. Rev. B **7**, 5212 (1973).

[50] M. P. Allen and D. J. Tildesley, *Computer Simulation of Liquids* (Oxford Science Publications, New York, 1987), p. 385.

[51] J. R. Smyth, R. J. Swope, and A. R. Pawley, Am. Mineral. **80**, 454 (1995).

[52] E. Kim, P. F. Weck, and T. R. Mattsson, J. Appl. Phys. **124**, 035903 (2018).

[53] P. F. Weck, K. R. Cochrane, S. Root, J. M. D. Lane, L. Shulenburger, J. H. Carpenter, T. Sjostrom, T. R. Mattsson, and T. J. Vogler, Phys. Rev. B **97**, 125106 (2018).

[54] P. F. Weck, J. P. Townsend, K. R. Cochrane, S. D. Crockett, and N. W. Moore, J. Appl. Phys. **125**, 245905 (2019).

[55] E. P. Meagher and G. A. Lager, Can. Mineralogist **17**, 77 (1979).

[56] C. J. Howard, T. M. Sabine, and F. Dickson, Acta Crystallogr., Sect. B: Struct. Sci. **47**, 462 (1991).

[57] S. N. Luo, A. Strachan, and D. C. Swift, J. Chem. Phys. **120**, 11640 (2004).

[58] M. J. O'Neil, *The Merck Index: An Encyclopedia of Chemicals, Drugs, and Biologicals.*, 15th ed. (Royal Society of Chemistry, Cambridge, UK, 2013), p. 1755.

[59] R. W. Woolfolk, M. Cowperthwaite, and R. Shaw, Thermochim. Acta **5**, 409 (1973).

[60] M. Millot, Phys. Plasmas **23**, 014503 (2016).

[61] Y. Laudernet, J. Clérouin, and S. Mazevet, Phys. Rev. B **70**, 165108 (2004).

[62] N. A. Dubrovinskaia, L. S. Dubrovinsky, R. Ahuja, V. B. Prokopenko, V. Dmitriev, H. P. Weber, J. M. Osorio-Guillen, and B. Johansson, Phys. Rev. Lett. **87**, 275501 (2001).